

Near-infrared III-nitride-on-silicon nanophotonic platform with microdisk resonators

I. Roland,¹ Y. Zeng,¹ X. Checoury,¹ M. El Kurdi,¹ S. Sauvage,¹ C. Brimont,² T. Guillet,² B. Gayral,^{3,4} M. Gromovyi,⁵ J. Y. Duboz,⁵ F. Semond,⁵ M. P. de Micheli,⁶ and P. Boucaud^{1,*}

¹*Institut d'Electronique Fondamentale, CNRS, Univ. Paris-Sud, Université Paris-Saclay, Bâtiment 220, Rue André Ampère, F-91405 Orsay, France*

²*Laboratoire Charles Coulomb (L2C), UMR 5221 CNRS-Université de Montpellier, F-34095 Montpellier, France*

³*Université Grenoble Alpes, F-38000 Grenoble, France*

⁴*CEA, INAC-PHELIQS, Nanophysique et semiconducteurs group, F-38000 Grenoble, France*

⁵*Centre de Recherche pour l'Hétéro-Epitaxie et ses Applications (CRHEA)-CNRS, Rue Bernard Gregory, F-06560, Valbonne, France*

⁶*Laboratoire de Physique de la Matière Condensée, UMR CNRS 7336, Université de Nice-Sophia Antipolis, 06100 Nice, France*

[*philippe.boucaud@ief.u-psud.fr](mailto:philippe.boucaud@ief.u-psud.fr)

<http://pages.ief.u-psud.fr/QDgroup>

Abstract: We have developed a nanophotonic platform with microdisks using epitaxial III-nitride materials on silicon. The two-dimensional platform consists of suspended waveguides and mushroom-type microdisks as resonators side-coupled with a bus waveguide. Loaded quality factors up to 80000 have been obtained in the near-infrared spectral range for microdisk diameters between 8 and 15 μm . We analyze the dependence of the quality factors as a function of coupling efficiency. We have performed continuous-wave second harmonic generation experiments in resonance with the whispering gallery modes supported by the microdisks.

© 2016 Optical Society of America

OCIS codes: (230.5750) Resonators; (250.5300) Photonic integrated circuits; (250.4390) Non-linear optics, integrated optics.

References and links

1. H. Jung, R. Stoll, X. Guo, D. Fischer, and H. X. Tang, "Green, red, and IR frequency comb line generation from single IR pump in AlN microring resonator," *Optica* **1**, 396–399 (2014).
2. C. Xiong, W. H. P. Pernice, X. Sun, C. Schuck, K. Y. Fong, and H. X. Tang, "Aluminum nitride as a new material for chip-scale optomechanics and nonlinear optics," *New J. Phys.* **14**, 095014 (2012).
3. D. Sam-Giao, D. Néel, S. Sergent, B. Gayral, M. J. Rashid, F. Semond, J. Y. Duboz, M. Mexis, T. Guillet, C. Brimont, S. David, X. Checoury, and P. Boucaud, "High quality factor AlN nanocavities embedded in a photonic crystal waveguide," *Appl. Phys. Lett.* **100**, 191104 (2012).
4. S. Sergent, M. Arita, S. Kako, S. Iwamoto, and Y. Arakawa, "High-Q (≥ 5000) AlN nanobeam photonic crystal cavity embedding GaN quantum dots," *Appl. Phys. Lett.* **100**, 121103 (2012).
5. N. Vico Triviño, R. Butté, J.-F. Carlin, and N. Grandjean, "Continuous wave blue lasing in III-Nitride nanobeam cavity on silicon," *Nano Lett.* **15**, 1259–1263 (2015).
6. J. Sellés, C. Brimont, G. Cassaboïs, P. Valvin, T. Guillet, I. Roland, Y. Zeng, X. Checoury, P. Boucaud, M. Mexis, F. Semond, and B. Gayral, "Deep-UV nitride-on-silicon microdisk lasers," *Sci. Rep.* **6**, 21650 (2016).

7. C. Xiong, W. H. P. Pernice, and H. X. Tang, "Low-loss, silicon integrated, aluminum nitride photonic circuits and their use for electro-optic signal processing," *Nano Lett.* **12**, 3562–3568 (2012).
8. B. Thubthimthong, T. Sasaki, and K. Hane, "Asymmetrically and vertically coupled hybrid Si/GaN microring resonators for on-chip optical interconnects," *IEEE Photonics J.* **7**, 7801511 (2015).
9. C. Xiong, W. Pernice, K. K. Ryu, C. Schuck, K. Y. Fong, T. Palacios, and H. X. Tang, "Integrated GaN photonic circuits on silicon (100) for second harmonic generation," *Opt. Express* **19**, 10462–10470 (2011).
10. A. W. Bruch, C. Xiong, B. Leung, M. Poot, J. Han, and H. X. Tang, "Broadband nanophotonic waveguides and resonators based on epitaxial GaN thin films," *Appl. Phys. Lett.* **107**, 141113 (2015).
11. I. Roland, Y. Zeng, Z. Han, X. Checoury, C. Blin, M. El Kurdi, A. Ghrib, S. Sauvage, B. Gayral, C. Brimont, T. Guillet, F. Semond, and P. Boucaud, "Near-infrared gallium nitride two-dimensional photonic crystal platform on silicon," *Appl. Phys. Lett.* **105**, 011104 (2014).
12. Y. Zeng, I. Roland, X. Checoury, Z. Han, M. El Kurdi, S. Sauvage, B. Gayral, C. Brimont, T. Guillet, M. Mexis, F. Semond, and P. Boucaud, "Resonant second harmonic generation in a gallium nitride two-dimensional photonic crystal on silicon," *Appl. Phys. Lett.* **106**, 081105 (2015).
13. N. Vico Triviño, M. Minkov, G. Urbinati, M. Galli, J.-F. Carlin, R. Butté, V. Savona, and N. Grandjean, "Gallium nitride L3 photonic crystal cavities with an average quality factor of 16900 in the near infrared," *Appl. Phys. Lett.* **105**, 231119 (2014).
14. F. Semond, "Epitaxial challenges of GaN on silicon," *MRS Bulletin* **40**, 412–417 (2015).
15. M. Mexis, S. Sergent, T. Guillet, C. Brimont, T. Bretagnon, B. Gil, F. Semond, M. Leroux, D. Néel, S. David, X. Chécoury, and P. Boucaud, "High quality factor nitride-based optical cavities: microdisks with embedded GaN/Al(Ga)N quantum dots," *Opt. Lett.* **36**, 2203–2205 (2011).
16. P. S. Kuo, J. Bravo-Abad, and G. S. Solomon, "Second-harmonic generation using 4bar-quasi-phasematching in a GaAs whispering-gallery-mode microcavity," *Nat. Commun.* **5**, 3109 (2014).
17. Q. Li, A. A. Eftekhar, Z. Xia, and A. Adibi, "Azimuthal-order variations of surface-roughness-induced mode splitting and scattering loss in high-Q microdisk resonators," *Opt. Lett.* **37**, 1586–1588 (2012).
18. S. Blaize, F. Gesuele, I. Stefanon, A. Bruyant, G. Léronnel, P. Royer, B. Martin, A. Morand, P. Benech, and J.-M. Fedeli, "Real-space observation of spectral degeneracy breaking in a waveguide-coupled disk microresonator," *Opt. Lett.* **35**, 3168–3170 (2010).
19. A. Yariv, "Universal relations for coupling of optical power between microresonators and dielectric waveguides," *Electron. Lett.* **36**, 321–322 (2000).
20. M. Borselli, K. Srinivasan, P. E. Barclay, and O. Painter, "Rayleigh scattering, mode coupling, and optical loss in silicon microdisks," *Appl. Phys. Lett.* **85**, 3693–3695 (2004).
21. M. Soltani, "Novel integrated silicon nanophotonic structures using ultra-high Q resonator," Ph.D. thesis, Georgia Institute of Technology (2009).
22. Z.-F. Bi, A. W. Rodriguez, H. Hashemi, D. Duchesne, M. Loncar, K.-M. Wang, and S. G. Johnson, "High-efficiency second-harmonic generation in doubly-resonant $\chi(2)$ microring resonators," *Opt. Express* **20**, 7526–7543 (2012).
23. M. Borselli, "High-Q microresonators as lasing elements for silicon photonics," Ph.D. thesis, California Institute of Technology (2006).
24. M. L. M. Balistreri, D. J. W. Klunder, F. C. Blom, A. Driessen, H. W. J. M. Hoekstra, J. P. Korterik, L. Kuipers, and N. F. van Hulst, "Visualizing the whispering gallery modes in a cylindrical optical microcavity," *Opt. Lett.* **24**, 1829–1831 (1999).
25. I.-W. Feng, W. Zhao, J. Li, J. Lin, H. Jiang, and J. Zavada, "Correlation between the optical loss and crystalline quality in erbium-doped GaN optical waveguides," *Appl. Opt.* **52**, 5426–5429 (2013).

1. Introduction

III-nitride materials on silicon present a very high interest for photonics from the near-infrared to the ultra-violet spectral range. As wide bandgap semiconductors, the III-nitride semiconductors like AlN or GaN have a very large transparency window. They exhibit a second-order non linear susceptibility that can be exploited for electro-optics Pockel's effects, harmonic generation experiments and comb generation when using a combination of second and third order non linear susceptibilities [1]. The mechanical properties of AlN offer the possibility to fabricate high-frequency opto-mechanical resonators [2]. In the visible or UV spectral range, active layers can be embedded in nanophotonic structures thus leading to light emitting diodes or lasers [3–6]. The direct growth of the III-nitride materials on silicon allows one to benefit from a low-cost large-scale platform. The selective etching properties between nitride materials and silicon make the fabrication of suspended structures straightforward.

To take advantage of the specificities of the III-nitride semiconductors for photonics, one

has to develop two-dimensional photonic circuits for light routing and for efficient in- and out-coupling of light with these circuits. Advanced results were obtained for photonic circuits with sputtered AlN on oxide with the achievement of quality factors up to 600000 around 1.55 μm with microring resonators of 80 μm diameter [7]. Using an hybrid GaN-on-silicon bonding technology, loaded quality factors up to 40000 were obtained in the near-infrared with 40 μm diameter microrings [8]. With epitaxial GaN on silicon, high quality factors are more difficult to achieve because of stronger residual absorption and scattering associated with interface defects. Quality factors of 10000 were obtained with large microrings fabricated with bonding after epitaxial growth [9], recently improved to intrinsic quality factors of 71000 for 80 μm microrings with GaN grown on sapphire [10]. For resonators with a much smaller volume, quality factors up to 34000 were obtained with photonic crystal resonators on a silicon platform [11,12] as well as up to 22000 in [13]. No results have been reported for small diameter III-nitride-on-silicon microdisks.

In this article, we demonstrate a two-dimensional nanophotonic platform consisting of suspended waveguides and microdisk resonators. The structures are fabricated from GaN/AlN layers grown on silicon. We report quality factors up to 80000 in the near-infrared (1500-1620 nm), for microdisks diameters varying between 8 and 15 μm , i.e. much smaller diameters as compared to previous reports. We analyze the dependence of the quality factors as a function of the coupling between the side-waveguides and the microresonators. We have performed second harmonic generation experiments with a continuous wave excitation. This allows us to collect the frequency-doubled signal at 2ω , which maps the spatial profile of the resonant modes at ω . The diffraction limit being twice as small at 2ω than at ω , this allows a direct observation of the resonant modes in a far-field experiment with a much better spatial resolution than direct observation at ω . We can in particular identify the modes from their radial antinodes in such an experiment.

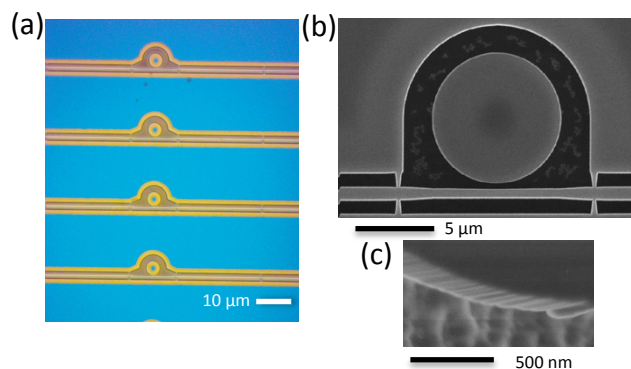


Fig. 1. (a) Optical microscopy image of a series of microdisks and their coupling waveguides. The color contrast results from the underetching. (b) Scanning electron microscopy image of a 8 μm diameter nitride microdisk and its suspended side-coupling bus waveguides. One can observe the nanotethers that maintain the coupling waveguide. The clearer zones correspond to underetched regions. The pedestal can be observed with a darker contrast at the disk center. (c) Zoom image of the microdisk sidewall

II. Sample fabrication

The studied samples were fabricated following the same process as for the III-nitride on silicon two-dimensional photonic crystal platform [11]. The III-nitride layers were grown by molec-

ular beam epitaxy on Si(111) substrates [14]. They consist of a 50 nm thick AlN layer first grown on Si, followed by a 280 nm thick GaN layer. The total thickness is close to $\frac{\lambda}{2n}$ thickness where n is the refractive index of the nitride material. The processing was performed using a combination of electronic beam lithography with UV-3 photoresist and chlorine-based inductively coupled plasma etching. Dry etching was achieved at a global pressure of 12 mTorr with 25 standard cubic centimeters per minute (sccm) Cl₂, 10 sccm BCl₃ and 5 sccm Ar. The global length of the structure is 500 μm . Straight waveguides are suspended by nanotethers on both sides of the waveguides. The spacing between the tethers is around 25 μm with a stochastic variation around this mean position to avoid resonant interference effects along the waveguide. There are 18 pairs of tethers along the structure. The size of the tethers at the junction with the waveguides is 100 nm. The nominal width of the waveguide is 600 or 700 nm except close to the microdisk resonator where it is 450 nm large. Light is coupled in the photonic circuit through inverted tapers with a length of 12 μm . The width of the taper apex is around 100 nm. The global transmission losses from lensed fiber to lensed fiber are 13 dB in TE polarization. These transmission losses can be decomposed in 3 dB loss for each taper and 7 dB losses due to the scattering at the nanotethers. The microdisk resonators have a diameter that varies between 8 and 15 μm . The fabrication of the suspended-waveguides and mushroom-type microdisks was achieved following a XeF₂ selective etching between the nitride material and the silicon substrate [15]. The underetching depth is between 2 and 3 μm . Figure 1(a) shows an optical microscope image of a fraction of the structure where a succession of microdisks and bus waveguides can be observed. Figure 1(b) shows a scanning electron microscopy image of 8 μm diameter nitride microdisk with its side-coupling bus waveguide. The distance between the microdisk and the waveguide was varied from 350 to 1100 nm, thus allowing to finely tune the coupling regime between both structures. This tuning control by design is a real advantage for integrated platforms as compared to the coupling approach using an external fiber [16]. Figure 1(c) shows a zoomed view of the microdisk sidewall. The roughness is very limited and difficult to estimate precisely quantitatively. We observe a ripple with a period in the hundred of nm range.

III. Microdisk optical characterization

Figures 2(a) and 2(b) show the transmission spectra of structures with 8 and 15 μm diameter microdisks respectively. The coupling distance between the microdisk and the side-waveguide is 550 and 350 nm for each structure. One observes marked resonances that correspond to the coupling to whispering gallery modes in the microdisks. The free spectral range is 44 nm for the 8 μm microdisks and decreases to 23 nm for the 15 μm microdisk. This free spectral range is in excellent agreement with the one that can be calculated using a finite-difference time-domain (FDTD) formalism when considering a refractive index of 2.04 for the AlN layer and 2.29 for the GaN layer in TE polarization at 1.55 μm . For the 8 μm microdisk, the modes at 1579 and 1583 nm are attributed to the TE(2,20) and TE(1,24) modes respectively where the first integer n represents the radial order (n radial antinodes along one disk radius) and the second integer m represents the azimuthal order ($2m$ antinodes along one disk perimeter). All modes stem from the fundamental TE mode characterized by one antinode along the z direction. Their experimental spectral positions are in excellent agreement with those calculated (1578 nm and 1583 nm respectively). The best quality factors that have been obtained with these structures are shown in Fig. 2(c) and 2(d). In the latter case, the air gaps between the microdisk and the waveguide are 1050 and 850 nm, allowing to obtain better quality factors but smaller transmission dips as compared to Figs. 2(a) and 2(b). The modes are split and the resonances correspond to a linear combination of clockwise and counter-clockwise propagating modes. We attribute this splitting to the scattering due to the sidewall surface roughness of the disk

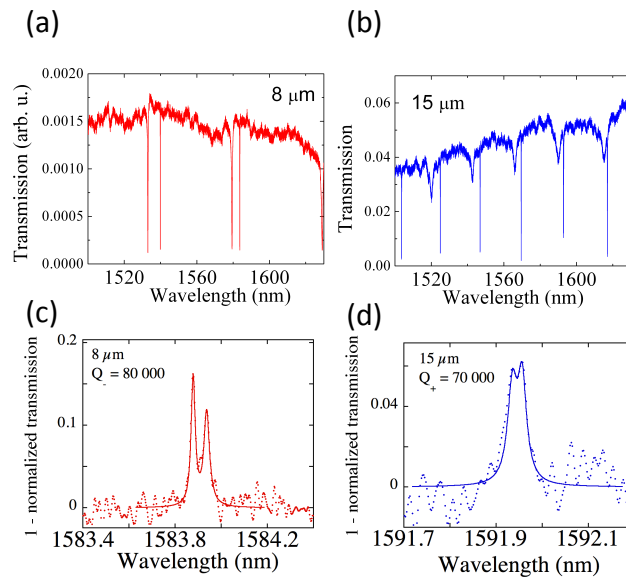


Fig. 2. (a) Transmission spectrum of a 8 μm diameter microdisk with a gap distance between microdisk and waveguide of 550 nm. (b) Transmission spectrum of a 15 μm diameter microdisk. Gap distance 350 nm. (c) Zoom around the resonances (1 - normalized transmission) at 1583.9 nm for a gap distance of 1050 nm (different from Fig.(a)) for the 8 μm diameter microdisk. The Lorentzian fits gives a loaded quality factor up to 80000. (d) Zoom around the resonances at 1592 nm for a gap distance of 850 nm (different from Fig.(b)) for the 15 μm diameter microdisk. The Lorentzian fit gives a loaded quality factor up to 70000.

and eventually from an asymmetry in the disk [17]. The magnitude of the splitting varies from disk to disk. As the splitting can be significant even when the gap between bus waveguide and microdisk is large, we do not attribute the splitting to a coupling with the waveguide mode [18]. The loaded quality factors that are measured in these structures are 80000 and 70000 for the 8 and 15 μm microdisks. We have obtained similar results on disks with a 12 μm diameter and different series of fabrication batches. These quality factors are the largest measured so far at these wavelengths with epitaxial GaN on Si and are obtained in structures with a small diameter as compared to the 80 μm ring diameter reported in [10] with GaN on sapphire. They are also much larger than those obtained with photonic crystal structures [11], although the modal volume is significantly larger.

Figure 3(a) shows the dependence of the loaded quality factor for the 15 μm microdisk as a function of the gap distance measured for the mode at 1592 nm. The quality factor increases steadily, as expected, as the distance increases. We have also measured the transmission amplitude of the resonance as a function of the gap distance. One observes a regular decrease of this amplitude for gap distances above 400 nm. Similar results were also obtained on structures with different diameters. The regular decrease of the transmission variation is explained by the following features. There are three quality factors that need to be considered for the transmission: the intrinsic quality factors of the microdisk, Q_{int} , the coupling factor that results from the overlap between the waveguide mode and the whispering gallery mode, Q_c , and the quality factor, Q_{split} , that results from the splitting between the clockwise and counter-clockwise propagating modes ($Q_{split} = \frac{\omega_0}{\Delta\omega_{peak}}$ where $\Delta\omega_{peak}$ is the frequency difference between both res-

onances). When there is no lifting of degeneracy, Q_{split} tends to infinite, and the coupling to the microdisk is maximum when $Q_{int} = Q_c$ [19]. In the latter case, the loaded quality factor corresponds to half the value of Q_{int} . When a splitting is present, the transmission amplitude can be calculated from coupled modes equations accounting for the presence of clockwise and counter-clockwise modes [20,21] and this gives the formula 1 where Q_+ and Q_- are the loaded quality factors of the split resonances ($\frac{1}{Q_{\pm}} = \frac{1}{Q_{int\pm}} + \frac{1}{Q_c}$)

$$T = \left| 1 - \frac{\frac{1}{Q_c} (4j \frac{(\omega - \omega_0)}{\omega_0}) + \frac{1}{Q_+} + \frac{1}{Q_-}}{(j [\frac{2(\omega - \omega_0)}{\omega_0}] - \frac{1}{Q_{split}}) + \frac{1}{Q_+}} (j [\frac{2(\omega - \omega_0)}{\omega_0}] + \frac{1}{Q_{split}}) + \frac{1}{Q_-}} \right|^2 \quad (1)$$

The critical coupling is achieved when $\frac{1}{Q_c} = \frac{1}{Q_{int}^2} + \frac{1}{Q_{split}^2}$. When Q_{split} is small as compared to Q_{int} , the critical coupling is thus obtained when Q_c is of the same order as Q_{split} . As the experimental lower value of Q_{split} is around 15000 for the microdisks (value measured for the 15 μm diameter microdisk and a gap of 550 nm - 18000 for a gap of 350 nm), one expects a maximum transmission variation for Q_c around 15000-20000 and a regular decrease of transmission variation at larger gap distances, as observed experimentally. From this modeling, we can deduce the dependence of Q_c as a function of the gap distance. Q_c increases exponentially as a function of the distance as shown in the inset of Fig. 3(b). All measurements reported in Fig. 3(a) are thus obtained in the undercoupled regime. By combining the measurements between Figs. 3(a) and 3(b), we deduce an intrinsic quality factor that can vary between 40000 and 71000 in this example, the 71000 value being obtained for the larger gap distance.

The maximum quality factors were obtained with modes that show a splitting between the clockwise and counter-clockwise propagating modes. In Fig. 2(b), the mode at 1586 nm for the 15 μm microdisk has a significantly smaller quality factor. In order to experimentally identify the origin of the modes, we have performed, in addition to FDTD calculations, resonant second harmonic generation experiments with these microdisks. The experiments are performed at room temperature with a continuous wave source using the same set-up as reported in [12]. The second harmonic is collected perpendicularly to the microdisk plane with a microscope objective (NA 0.9) and the radiated pattern is imaged using an electron multiplying camera. We have not attempted to achieve phase-matched second harmonic generation in these microdisks and/or high conversion efficiency [22] and the harmonic generation is uniquely enhanced by the resonance of the pump mode.

Figure 4 summarizes the results obtained by second harmonic generation. Figure 4(a) shows the transmission of the microdisk measured in TE polarization with a gap distance of 450 nm. Figure 4(b) shows the optical image of the microdisk under white light illumination measured with the same set-up that collects the harmonic. Figures 4(c) and 4(d) correspond to the spatial profiles for an excitation at 1588 nm and 1592 nm respectively. The spatial profiles are strikingly different. For the excitation at 1588 nm corresponding to a low quality factor mode, the profile is dominated by a ring located inside the microdisk and close to the microdisk periphery. One also observes a more diffuse ring with a smaller diameter inside the microdisk and weaker additional features inside and outside of the microdisk that result from the propagation of the harmonic polarization [12]. For the mode excited at 1592 nm, there are clearly two rings composed of multiple lobes, in particular for the inner ring in Fig. 4(d). Both rings have similar amplitudes with the largest ring slightly at the outer periphery of the microdisk while the inner pattern is inside the microdisk. The same spatial profile is obtained for both split resonances that correspond to the standing wave created from the combination of clockwise and counter-clockwise propagating modes. The standing wave of the fundamental mode can excite both clockwise and counter-clockwise modes at the harmonic frequency, the low frequency mode having more energy in the high dielectric region while the high frequency mode has more

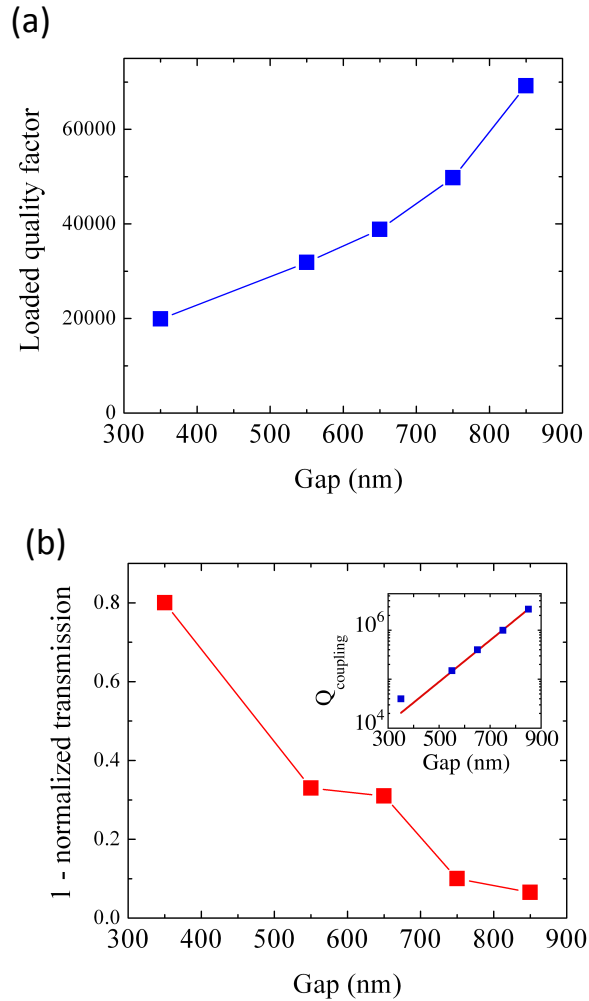


Fig. 3. (a) Dependence of the quality factor for the resonance at 1592 nm for the 15 μm diameter microdisk as a function of the gap distance between waveguide and microdisk. (b) Variation of the peak amplitude (1 - normalized transmission) as a function of the gap distance. The inset shows the value of Q_c in log scale as deduced from formula 1. One obtains an exponential dependence of Q_c vs. gap distance, as expected and illustrated by the full line.

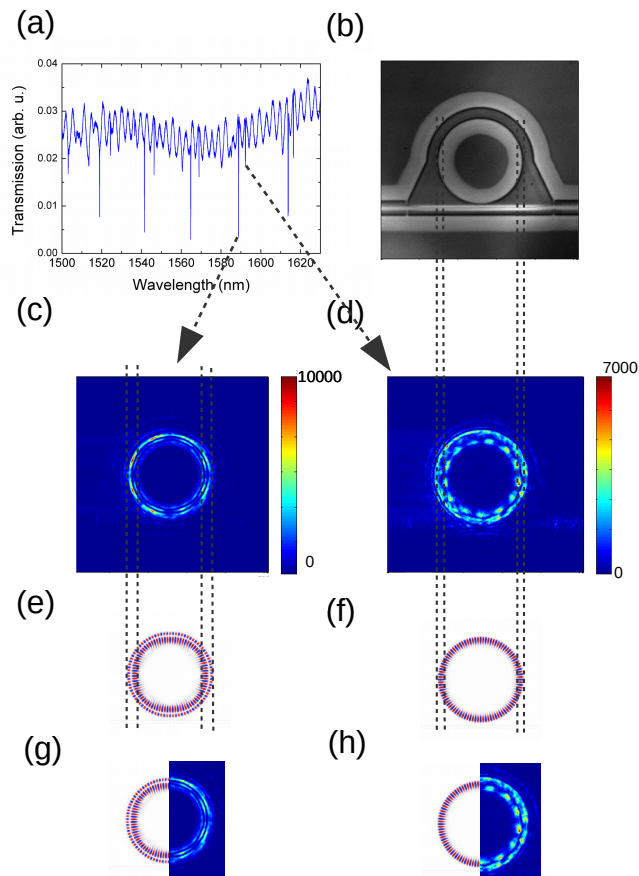


Fig. 4. (a) Transmission for a $15\ \mu\text{m}$ diameter microdisk with a gap distance of $450\ \text{nm}$. (b) optical microscopy image measured with the same set-up as the one used for the collection of second harmonic generation. (c) Profile of the second harmonic radiated pattern for the mode at $1586\ \text{nm}$ with a low quality factor. The laser power is $13\ \text{dB}$. (d) Profile of the second harmonic radiated pattern for the mode at $1592\ \text{nm}$ with a high quality factor. These modes are those that provide the highest quality factors. (e) Near-field H_z profile of the second-order radial mode $\text{TE}(2,43)$. (f) Near-field H_z profile of the first-order radial mode $\text{TE}(1,48)$. The dashed lines are guide to the eyes to highlight the disk periphery and the average radial positions of the lobes. (g) and (h) Superimposed images of the near-field and second harmonic patterns

energy in air [23]. The occurrence of lobes results from a spatial beating between the excited harmonic modes with different propagation constants [24]. We also show in Figs. 4(e) and 4(f) the near-field profiles of the second-order TE(2,43) and first-order TE(1,48) radial modes calculated for these microdisks by finite difference time domain calculations at 1588 and 1592 nm respectively. Superimposed near-field and second harmonic patterns are shown in Figs. 4(g) and 4(h). The spectral positions of the different modes are in agreement with those calculated by FDTD. We associate the pattern observed in Fig. 4(d) to the one generated by the first order radial mode [16] while the pattern shown in Fig. 4(c) is associated with the second-order radial mode. For both configurations, the average radial positions of the main rings correspond to those calculated by FDTD for the near-infrared modes that represent the source terms generating the second-order polarization. Only the second-order radial mode can generate significant harmonic at 1.6 μm from the disk periphery due to its second-order radial lobe. We note that the ability to observe these features is a consequence of the higher spatial resolution achieved with the harmonic as compared to the pump mode. This mode identification was confirmed by performing measurements using disks with different underetching lengths. The second-order radial mode can only be observed when the underetching is above 2.5 μm . The first order radial modes are those that exhibit the largest quality factors. On the contrary, the second-order radial modes are limited by their interaction and absorption with the microdisk pedestal. In the latter case, the maximum quality factors for the higher-order radial modes are measured around 20000-30000 whereas they can be as large as 80000 for the first-order radial mode.

There are different factors that limit the quality factors: i. the scattering linked to the epitaxial material and the defects generated when growing nitride on silicon [25]. ii. the asymmetry of the structures due to AlN/GaN stacking and the coupling between TE and TM modes induced by this asymmetry. iii. the side-wall roughness of the microdisks and possibly the surface roughness due to underetching of N-polarity bottom nitride surface. We will attempt in future experiments to further increase the quality factors by minimizing the influence of these different features.

IV. Conclusion

In conclusion, we have reported on a near-infrared III-nitride-on-silicon nanophotonic platform with microdisks as resonators. We have obtained quality factors up to 80000 in the near-infrared spectral range for disk diameters varying between 8 and 15 μm . We have shown that the coupling efficiency in the microdisk is controlled by the gap distance between the disk resonator and the bus waveguide and that the maximum coupling efficiency is obtained for a coupling quality factor close to the quality factor associated with the splitting between clockwise and counter-clockwise propagating modes. We have analyzed the whispering gallery modes through their second harmonic generation radiated patterns. This III-nitride-on-silicon photonic platform is well suited for performing further nonlinear experiments with a near-infrared pump. It can also be down-scaled to reach by design the visible range or the ultra-violet spectral range.

Acknowledgments

The authors acknowledge support from the projects GANEX (ANR-11-LABX-0014) and QUANONIC (ANR-13-BS10-0010). GANEX belongs to the public funded 'Investissements d'Avenir' program managed by the French ANR agency. This work was partly supported by the RENATECH network. This work is also partially supported by a public grant overseen by the French National Research Agency (ANR) as part of the "Investissements d'Avenir" program (Labex NanoSaclay, reference: ANR-10-LABX-0035).